Environmental Science Processes & Impacts

ROYAL SOCIETY OF CHEMISTRY

PAPER

View Article Online
View Journal | View Issue

Cite this: *Environ. Sci.: Processes Impacts*, 2026, **28**, 1374

Image-based observation of aerosol hygroscopic growth and extinction coefficient reversal at three wavelengths, supported by Köhler theory simulations

Juhyeon Sim, [a] Juseon Shin, [a] Yunki Mun, [a] Naghmeh Dehkhoda, [a] Sohee Joo, [a] Dukhyeon Kim [b] and Youngmin Noh *[a]

As relative humidity (RH) increases, aerosols take up water and grow. This changes their size and refractive index, affecting light scattering and absorption. Such changes can bias comparisons between remote sensing and *in situ* measurements. We simulated hygroscopic growth effects on extinction coefficients and the Ångström exponent (AE) at 459, 534, and 600 nm using Köhler–Mie theory. Ammonium sulfate ($\kappa = 0.53$) was used as the representative aerosol composition. The Kelvin effect suppressed the growth of sub-0.1 μm particles by a factor of ~4 at RH > 80%. Fine-mode particles were used as a representative aerosol composition in the simulations. Fine-mode particles dominated total extinction, contributed 93.2% at 90% RH. Extinction coefficients reversed their spectral ordering near RH ~98% in simulations and ~92% in observations, producing negative AE. We also retrieved extinction coefficients and AE from RGB camera images during fog dissipation in Daejeon, South Korea. The observed AE became negative at high RH and returned to positive values as aerosols dried, consistent with simulations. These results show that image-based methods can capture hygroscopic growth and highlight the importance of RH-dependent corrections for reconciling remote sensing and *in situ* observations.

Received 10th October 2025
Accepted 30th March 2026

DOI: 10.1039/d5em00826c

rsc.li/espi

Environmental significance

This study integrates Köhler theory and Mie scattering simulations to investigate aerosol hygroscopic growth and its wavelength-dependent optical effects. We validate theoretical predictions through RGB image-based observations during natural fog events, demonstrating that image-based methods can capture hygroscopic growth impacts on extinction coefficients and Ångström exponent variations. The observed wavelength-dependent changes demonstrate the importance of considering humidity effects in atmospheric optical modeling and remote sensing applications. This approach offers enhanced spatial and temporal coverage for monitoring aerosol hygroscopic behavior, supporting improved visibility predictions and air quality measurement. The consistency between theoretical simulations and field observations validates the utility of cost-effective imaging techniques for atmospheric aerosol studies, supporting better air quality assessments and climate model predictions under varying humidity conditions.

Introduction

The significance of atmospheric aerosols in climate change research and air quality management is well established, leading to extensive investigations into their physical properties and chemical compositions.[1–6] Aerosol hygroscopic growth has been recognized as a fundamental atmospheric process since the early work of Köhler (1936), who established the theoretical foundation for understanding water vapor condensation on aerosol particles.[7] The hygroscopic behavior of atmospheric aerosols significantly affects their size distribution, optical properties, and cloud condensation nucleus (CCN) activity.[8,9] Early investigations focused on single-component systems, with Tang and Munkelwitz (1994); Tang and Munkelwitz (1993) conducting pioneering laboratory studies on the hygroscopicity of various inorganic salts common in atmospheric aerosols.[10,11] The complexity of atmospheric aerosols, comprising multiple chemical components with varying hygroscopicity, led to the development of simplified parameterization schemes. Kreidenweis *et al.* (2005) introduced the concept of volume-weighted hygroscopicity, later refined by Petters and Kreidenweis (2007) into the single-parameter κ(kappa)-framework, which has since been widely adopted to characterize the hygroscopic properties of ambient aerosols.[8,12–15]

[a]*Division of Earth and Environmental System Science, Pukyong National University, Busan, 48513, Republic of Korea. E-mail: nym@pknu.ac.kr*
[b]*School of Basic Science, Hanbat National University, Daejeon, 34158, Republic of Korea*

The interaction between aerosol particles and electromagnetic radiation has been extensively studied since the foundational work of Mie (1908), who provided exact solutions for light scattering by spherical particles.[16] Mie theory remains the cornerstone for calculating aerosol optical properties, including scattering and absorption cross-sections, asymmetry parameters, and phase functions.[17,18] The wavelength and size dependence of aerosol extinction has been parameterized using the AE, first introduced by Ångström (1929) for atmospheric turbidity measurements.[19] The Ångström exponent (AE) provides valuable information about aerosol size distribution, with higher values indicating smaller particles and lower values suggesting larger particles.[20,21] However, the relationship between AE and aerosol properties becomes complex in the presence of bimodal or multimodal size distributions.[22,23] Hygroscopic growth significantly modifies aerosol optical properties by altering both the particle size and refractive index. The effective refractive index of hydrated particles approaches that of water ($n = 1.33$) as the water content increases.[24,25] This dual effect—an increase in size and decrease in refractive index—leads to complex wavelength-dependent changes in extinction efficiency that cannot be predicted from simple scaling relationships.[26,27] These measurements have revealed the importance of aerosol chemical composition, mixing state, and morphology in determining hygroscopic behavior.[28,29] Field observations have shown that hygroscopic growth can increase aerosol light scattering by factors of 1.5–4 at high relative humidity.[24,30,31]

The Kelvin effect, which describes the influence of surface curvature on equilibrium vapor pressure, becomes increasingly important for particles smaller than approximately 100 nm.[32] This effect limits the hygroscopic growth of small particles and affects their CCN activation behavior.[8,33] Recent studies have incorporated curvature effects into hygroscopic growth models, showing improved agreement with observations for submicron particles.[34,35] The surface tension of aerosol solutions also varies with composition and concentration, influencing both the Kelvin effect and hygroscopic growth behavior.[36,37] Organic surfactants, in particular, can significantly reduce surface tension and alter growth characteristics.[38] Understanding these mechanisms is therefore essential for interpreting aerosol optical behavior under humid atmospheric conditions. Despite significant advances in understanding aerosol hygroscopic growth and its optical implications, several knowledge gaps remain. Most existing studies focus on laboratory characterization or point measurements, providing limited spatial and temporal coverage of real-world hygroscopic growth events. Moreover, the complex wavelength-dependent effects of hygroscopic growth on extinction coefficients remain insufficiently characterized, especially for polydisperse aerosol populations under varying environmental conditions.

Fog formation is a prominent manifestation of aerosol–water interactions. As relative humidity (RH) increases, aerosols first grow hygroscopically; once supersaturation is reached, some particles activate into fog droplets.[39–42] Consequently, fog episodes provide a natural laboratory in which humidity-driven changes in particle size and composition directly affect bulk optical properties such as the extinction coefficient and the AE. The extinction coefficient (α), defined as the sum of scattering and absorption coefficients per unit path length, quantifies the total attenuation of light by aerosols.[18,32] The AE describes the spectral dependence of extinction, with higher values indicating smaller particles and lower values suggesting a coarser size distribution.[21,43]

To address these limitations, this study extended a previously developed method for deriving extinction coefficients from RGB camera images to examine wavelength-dependent changes in extinction coefficient induced by aerosol hygroscopic growth across a wider spatial domain, including during fog episodes. Furthermore, we conducted theoretical simulations to evaluate whether the observed variations in extinction and the AE can be attributed to hygroscopic particle growth under elevated RH conditions. The present work thus proposes a cost-effective, image-based method that retrieves wavelength-dependent extinction coefficients and AE from RGB camera observations over space and time, and compares their RH-driven variations with simulations to test consistency under real atmospheric conditions. Specifically, this research aims to: (1) simulate the RH dependence of multi wavelength aerosol extinction coefficients and AE for assumed size distributions and compositions; (2) develop and validate a cost-effective RGB image retrieval of extinction coefficients and AE during fog; (3) compare simulations with observations to quantify the roles of particle size and hygroscopicity in shaping optical changes; and (4) demonstrate the practicality of this approach for near-real-time monitoring under varying humidity.

Methods

Image analysis during hygroscopic growth

The extinction coefficient and AE were retrieved at 2 min intervals from images acquired at the observation site (latitude 36.42°, longitude 127.39°, and altitude approximately 70 m above sea level). Meteorological variables, including temperature and RH, were obtained from the Korea Meteorological Administration (KMA) 500 m gridded dataset at 5 min resolution. We used three contiguous 500 m grid cells: the first contained the camera images acquired at the observation site, and the next two lay along the camera's field of view, yielding an effective path length of 1 km. A commercial digital camera (NIKON D7500) was used to derive extinction coefficients at multiple wavelengths (600, 534, 459 nm as RGB, respectively), with settings of f/35, ISO 100, and 1/4 s exposure time.

We calculated the extinction coefficient by comparing brightness at different distances using four targets with similar reflectance, as well as the sky. For each target and the sky, a region of interest was defined, and the average of 1–10 dark-channel pixels was used (a simple dark-channel inspired approach) to minimize reflectance and illumination effects.[44] The AE was then derived by fitting the three per-channel extinction coefficients to $\ln \alpha = -\mathrm{AE} \ln(\lambda) + C$, where the slope AE was obtained by log-linear regression across the RGB wavelengths (459, 534, and 600 nm). For details of extinction coefficient measurements and AE retrieval using cameras, see previous studies.[45–47] Unlike previous studies, we focused on fog

conditions with visibility below 1 km and therefore used only targets within that range. Images were captured from 06:55 to 12:57 Korea Standard Time (KST) on 2 November 2022, covering the full period from fog presence to dissipation. Images taken before sunrise were excluded because lighting was not uniform across all targets. All images were saved in JPEG format without post-processing. The JPEG files contained automatic corrections (*e.g.*, white balance, gamma and contrast) applied by the camera.[48] However, extinction coefficients were estimated from brightness differences between distances rather than absolute intensity. Because all images were taken under identical settings, internal corrections had little effect on extinction coefficients and AE analysis.

Aerosol hygroscopic growth

The saturation pressure of water vapor is determined as the product of water activity (a_w) and the Köhler function, which incorporates the curvature effects (Kelvin effects) in aerosol–water droplet solutions.[8,32,35,49–51]

$$S = a_w \exp\left(\frac{4\sigma_{s/a} M_w}{RT\rho_w D}\right) \quad (1)$$

In eqn (1), S represents the saturation of atmospheric water, which is the RH, and a_w represents the water activity. Furthermore, $\sigma_{s/a}$, M_w, R, T, ρ_w, and D represent the surface tension at the air (a)–solution (s) interface, molar mass of water, gas constant (8.314 J K^{-1} mol^{-1}), temperature, water density, and diameter of the hygroscopic aerosol, respectively. $\sigma_{s/a}$ is determined by temperature and the chemical composition of the solute. a_w depends on the amount of dissolved solute. For pure water, $a_w = 1$, and it decreases as solute concentration increases. It can be expressed as shown in eqn (2);[52]

$$a_w = \frac{n_w}{n_w + \sum_i^N v_i n_s^i} \quad (2)$$

where n_w and n_s are the number of moles of water (w) and solute (s) in the hygroscopic aerosol, N is the number of solutes in the aerosol, and v_i is the volume of each solute. When the number of moles in eqn (2) is expressed in terms of volume, it can also be represented as shown in eqn (3).[8]

$$a_w = \frac{D^3 - {D_d}^3}{D^3 - {D_d}^3(1-k)} = \frac{V - V_d}{V - V_d(1-\kappa)}, \quad \kappa = \sum_i \varepsilon_i \kappa_i \quad (3)$$

where D is the wet aerosol diameter, and D_d is the dry aerosol diameter. The ratio $\frac{D}{D_d}$ is defined as the growth factor ξ, then $\frac{V}{V_d}$ can be considered as ξ^3. If we divide both the numerator and denominator of eqn (3) by V_d, we obtain $\frac{\frac{V_{wet}}{V_{dry}} - 1}{\frac{V_{wet}}{V_{dry}} - 1 + k}$. As $\frac{V}{V_d}$ is ξ^3, eqn (3) can be simplified to $\frac{\xi^3 - 1}{\xi^3 - 1 + k}$.

In eqn (3) ε_i is the volume fraction of a specific solute relative to that of the total dissolved solute, and κ_i is the unitless hygroscopic parameter of solute i. The parameter κ quantifies the solute's water uptake ability by relating the amount of absorbed water to the particle dry volume, thereby providing a single-value measure of hygroscopicity in the κ-Köhler framework. Because different constituents exhibit different κ_i values, numerous studies have reported κ_i for various aerosol types.[52]

κ can be represented as the weighted sum of volume fractions of individual species (i), as described by Petters and Kreidenweis (2007).[8] As the κ varies with changes in aerosol composition, determining the average κ for all aerosols in a specific region through simple measurements alone is not feasible. In this study, we introduced a method that uses arbitrarily assigned initial values to calculate the extinction coefficient after hygroscopic growth. The κ can also be accurately determined by comparing the calculated extinction coefficient with the measured extinction coefficient and iteratively reducing the error.[53,54]

Hygroscopic aerosol growth induces changes in the effective refractive indices of aerosols. The effective refractive index of the aerosols is expressed as the volume-weighted sum of the refractive indices of water and solute aerosols.[55]

$$n_{eff} = \frac{{D_{dry}}^3 n_\alpha + \left(D_w - D_{dry}\right)^3 n_w}{{D_{dry}}^3 + \left(D_w - D_{dry}\right)^3} \quad (4)$$

As the size of aerosols increases due to water uptake, their refractive index (n_a) approaches that of water ($n_w = 1.33 + 0.001i$). The refractive index of hygroscopic aerosols is equal to or lower than that of dry aerosols because water typically has a lower refractive index than most aerosols. The change in the refractive index and size of aerosol should be considered in the simulation of the growth factor ($\xi = \frac{D_w}{D_{dry}}$) for calculating the extinction coefficient.

The second term in the exponential function in eqn (1) represents the Kelvin effect, which illustrates the curvature effect of aerosols. It can be expressed as follows.[56]

$$\frac{4\sigma_{s/a} M_w}{RT\rho_w D} = \ln\left(\frac{P}{P_0}\right) \quad (5)$$

where P_0 is the saturation vapor pressure over a flat surface (no curvature) and P is the equilibrium saturation vapor pressure over a curved aerosol (Kelvin effect). As D decreases, curvature increases and the saturation vapor pressure over the aerosol becomes higher. Thus, a higher supersaturation is required for condensation on the aerosol surface. RH is defined with respect to the flat-surface saturation vapor pressure and is therefore independent of aerosol size. Consequently, at a given ambient RH, smaller aerosols tend to be in net evaporation, whereas larger or more hygroscopic aerosols can grow; their growth occurs only when the ambient RH exceeds the equilibrium RH of the aerosol. This size- and composition-dependent growth threshold explains why ultrafine-mode aerosols, which are

smaller than typical fine-mode particles, are less likely to grow.

The Kelvin effect is related to the aerosol curvature, so it is significant for fine-mode aerosols and varies depending on the aerosol type.[35] For example, the Kelvin diameter (D_k) for ammonium sulfate, calculated as $D_k = \frac{4\sigma_{s/a}M_w}{RT\rho_w}$, is approximately 2.2 nm.[8,57] The surface tension ($\sigma_{s/a}$) of aqueous aerosols in the atmosphere varies depending on the temperature and solubility state of the dissolved aerosol.[1]

$$\sigma_{s/a} = \sigma_0 + \sigma_T(T_0 - T) + \sigma_s\mu_s \quad (6)$$

In eqn (6), σ is the surface tension, and T is the temperature. The subscript "0" in surface tension (σ_0) is the reference state, while $\sigma_{s/a}$ is the air–liquid interface of the aerosol solution. σ_s is a function of molar concentration and T_0 is set to 273 K, which is the reference temperature. Finally, μ_s is the molar concentration of the solute.

In this paper, a solute refers to a dry aerosol and can be described as a function of size. σ varies depending on T and μ_s. while T is determined by the ambient environment, μ_s is influenced by the quantity and chemical properties of aerosols. In this study, we focused only on ammonium sulfate. Ammonium sulfate is primarily formed through reactions between ammonia and sulfuric acid, making it a major component of fine particulate matter (PM) in urban and industrial areas because of its high proportion in aerosol mass.[58,59] In particular, an observational study conducted in South Korean urban areas has reported that ammonium sulfate accounts for approximately 30% of $PM_{2.5}$ mass concentration, making it one of the largest single contributors to aerosol mass.[60] Furthermore, ammonium sulfate is one of the most extensively characterized hygroscopic aerosol species, with well-established optical properties and growth factors, making it a suitable representative species for hygroscopic aerosol modelling. The molar concentration of the aerosol solute (μ_s) is determined by the wet aerosol diameter after hygroscopic growth, which can be expressed as the ratio of the final (wet) size to the initial dry size under subsaturated conditions. With increasing water uptake, the volume fraction of water increases while the molar concentration of the solute decreases. μ_s can be obtained from the proportion of aerosols dissolved in the solution.

$$\mu_s = \frac{x_s}{M_s(1-x_s)}, \quad x_s = \frac{\rho_{dry}V_{dry}}{\rho_w(V_w - V_{dry}) + \rho_{dry}V_{dry}} = \frac{\rho_{dry}}{\rho_w(\xi^3 - 1) + \rho_{dry}} \quad (7)$$

Eqn (7) describes the solute mass fraction (x_s), which is required to determine μ_s. The x_s is calculated as the ratio of the solute (aerosol) mass to the total mass after hygroscopic growth, which comprises the original aerosol mass and the absorbed water mass.

In calculating μ_s for surface tension, when the size of the hygroscopic aerosol is below the critical value (deliquescence point), the amount of water is lower than that of the solute. This is because when moisture adheres to the aerosol, its effect is minimal if the amount of water is insufficient relative to the aerosol. In calculating μ_s for surface tension, where ξ was 1.26 or lower, the x_s was fixed at 0.65. This value corresponds to the solute mass fraction calculated from eqn (7) at $\xi = 1.26$ —the threshold before aerosol volume doubles—using the density of ammonium sulfate (1.77 g cm^{-3}) and water (1 g cm^{-3}). In this low-growth regime, the amount of absorbed water is insufficient to represent the particle as a well-developed aqueous solution for the purpose of the surface-tension calculation. This treatment is consistent with the concentrated ammonium sulfate regime reported by a previous study.[11]

In addition, when the amount of water was insufficient relative to the aerosol, aerosol growth did not occur, implying that the ratio of the hygroscopic aerosol diameter to the dry aerosol diameter remained the same. Consequently, both the ξ and the x_s were 1, causing the denominator of μ_s to become zero, making the calculation impossible. Therefore, cases below the critical threshold were excluded.

Once the aerosol exceeds the critical threshold and begins to absorb water, the interaction between the water and aerosol leads to a rapid change in the surface tension.[37] Thus, when the size of the hygroscopic aerosol exceeds the critical threshold, the increasing amount of absorbed water allows μ_s to be calculated based on the ratio of solute to solvent. The rapid aerosol size increase in hygroscopic growth above this threshold explains why fog aerosols suddenly increase over time. This phenomenon is discussed in the real-time monitoring of aerosol optical properties during hygroscopic growth.

As summarized in Fig. 1, the flowchart shows the process of predicting the size of the hygroscopic aerosols and calculating the extinction coefficient by considering the Kelvin effect. The initial inputs included the size and density of dry aerosols, κ, the RH in the hygroscopic growth state, and the refractive indices of aerosols and water. The x_s was determined using an arbitrarily chosen growth factor ($\xi = 1.14$).

To determine the size of the hygroscopic aerosols, the calculation began by obtaining the x_s based on the wet-to-dry size ratio. The solute mass fraction is a function of the ξ.

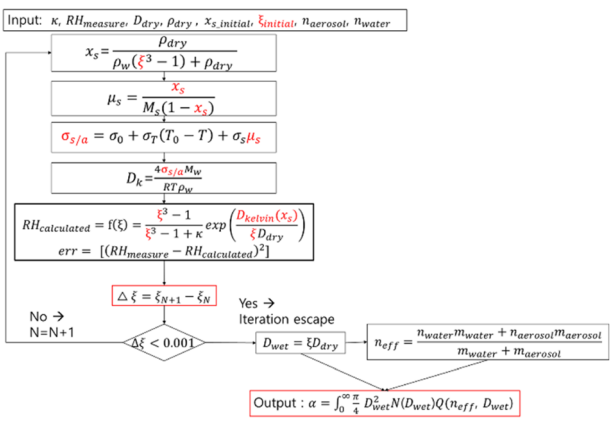

Fig. 1 Flowchart for aerosol size and extinction coefficient calculation during hygroscopic growth. Parameters highlighted in red were iteratively adjusted until residual converged.

Therefore, an initial arbitrary value ($\xi = 1.14$) was used to calculate the μ_s, which was then used to determine the surface tension. The calculated surface tension was incorporated into the curvature effect term to derive the D_k from which the RH was computed.

Next, the squared difference between the calculated RH and the input RH was determined to compute the residual sum of squares (RSS), which was then minimized to obtain the optimal aerosol ξ. This optimized ξ was then applied instead of the initial value, and the calculation process was repeated iteratively to update ξ. When the difference between the previously computed ξ and the newly calculated ξ was <0.001, the optimization was considered complete, and the obtained ξ was applied to the hygroscopic aerosol size distribution.

Using the aerosol growth ratio, the refractive index was calculated as a weighted average based on the volume fraction of each component (eqn (4)). Finally, the extinction coefficient was derived using the volume distribution after hygroscopic growth and the refractive index.

Characteristics of the extinction coefficient as a function of wavelength

The aerosol extinction coefficient (α) as a function of wavelength (λ) and refractive index (m) was calculated using Mie scattering theory, as follows:

$$\alpha(\lambda, m) = \int Q(r, \lambda, m)\pi r^2 N(r)\mathrm{d}r = \int Q_v(r, \lambda, m)V(r)\mathrm{d}r \quad (8)$$

In eqn (8), $Q(r, \lambda, m)$ is the extinction efficiency, and $Q_v(r, \lambda, m)$ is the volume extinction efficiency ($\frac{3}{4r}Q$), *i.e.*, the extinction cross-section per unit particle volume. At a given RH, the wet aerosol diameter is obtained as $D_w = \xi D_{dry}$, where ξ is the growth factor. The m is computed as a volume-weighted mixture of dry aerosol and water.[55] These parameters are then used to evaluate $\alpha(\lambda, m)$ from eqn (8). Here, $N(r)$ and $V(r)$ represent the number and volume size distribution of aerosols, respectively, as functions of particle radius r.

For the size distributions, we considered the fine- and coarse-mode peaks of aerosols. Although some studies also include nucleation or Aitken mode particles,[61] these contribute little to total extinction because of their very small volume extinction efficiency. Similarly, extremely large particles are negligible. Therefore, only the two dominant modes were considered.

Fig. 2 shows Q_v at the observed wavelengths along with the assumed aerosol volume size distribution. The distribution was based on a previous study's clean continental aerosol type characteristics.[62] This aerosol type was selected to reflect the regional characteristics of the study area, which is primarily residential with minimal industrial sources. Modal diameters of 0.21 μm and 2.63 μm were selected to represent fine and coarse particles, respectively, with geometric standard deviations of 1.61 and 1.90 for fine and coarse modes.[62] The relative volume concentrations between fine and coarse modes were adjusted to ensure realistic representation of local atmospheric conditions. This approach provides a representative size distribution for clean continental aerosol environments while maintaining consistency with regional observational characteristics.

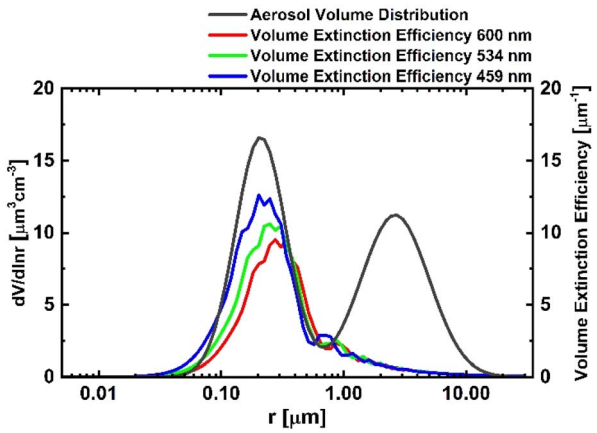

Fig. 2 Volume extinction efficiency and aerosol volume distribution by particle size.

Because site specific chemical composition data for Daejeon were not available, and no major local point sources are present, the aerosol ensemble was approximated as ammonium sulfate with a density of 1.77 g cm^{-3}.[63,64] Effective wavelengths of 600, 534, and 459 nm were used to calculate the volume extinction efficiency. As the wavelength increased, the efficiency peak shifted toward larger particle sizes, increasing sensitivity to coarse particles.

For very small particles ($r \leq 0.02$ μm), both particle volume and extinction efficient are low, while for very large particles ($r \geq 20$ μm), volume is significant but extinction efficiency is low. Consequently, contributions from these extremes are negligible. Even if coarse-mode aerosols increase further, their effect on extinction coefficient variability remains limited (Fig. 2).

AE is a qualitative indicator of aerosol size derived from the ratio of extinction coefficients at multiple wavelengths.[65] A higher fraction of larger particles typically leads to a lower AE, whereas a higher fraction of smaller particles increases the AE.[21]

In this study, simulations were performed at the effective wavelengths of the red, green, and blue (RGB) camera channels—600, 534, and 459 nm—to capture the hygroscopic growth state of atmospheric aerosols from camera images. Using these same wavelengths ensured consistency with the image-based extinction analysis.

$$\frac{\alpha_{\lambda_i}}{\alpha_{\lambda_B}} = \left(\frac{\lambda_i}{\lambda_B}\right)^{-AE} \quad i = R,\ G,\ B \quad (9)$$

In eqn (9), α_R, α_G, and α_B represent the extinction coefficient for each wavelength (R, G, and B), and λ is the effective wavelength (in nm).

Results

Hygroscopic growth and curvature effect of dry aerosols

Fig. 3 shows aerosol growth factors as a function of initial dry size and RH. In Fig. 3a, only water activity is considered,

whereas Fig. 3b includes both water activity and the curvature (Kelvin) effect. The first and second terms in eqn (1) describe these two influences: water activity depends on the κ and volume, while the exponential term accounts for curvature through surface tension.

Simulations were performed for initial aerosol diameters from 0.002 to 60 μm, assuming $\kappa = 0.53$ (ammonium sulfate; Petters & Kreidenweis (2007) and $T = 300$ K).[8] The size distribution followed typical atmospheric aerosol characteristics.[32,66] Without the curvature effect (Fig. 3a), all sizes showed similar monotonic growth with RH. When curvature was included (Fig. 3b), particles with diameter <2 μm grew less than 10% across the full RH range. This suppression occurs because the Kelvin term in eqn (1) does not approach zero for small sizes, limiting condensation.

Reduced growth in smaller particles is thus linked to curvature: as curvature increases, the RH required for condensation rises. Smaller particles with higher curvature, therefore have higher equilibrium vapor pressures, resulting in enhanced evaporation and reduced growth potential.

To quantitatively assess the suppression of hygroscopic growth by the curvature effect, Fig. 4 presents the ratio of the growth factor with the curvature effect to that without it, as a function of initial particle diameter and RH. When RH is below 40% or the aerosol diameters exceeds 10 μm, the two values show negligible difference and the ratio converges to unity. In contrast, when RH exceeds 80% and the particle diameter is smaller than 0.1 μm, the curvature effect leads to a difference of up to approximately four-fold. These results indicate that the curvature effect must be accounted for, particularly in the small particle regime, to accurately simulate hygroscopic growth of atmospheric aerosols. Using this framework, we simulated changes in aerosol volume distribution and extinction efficiency at 534 nm under varying RH. The distribution was based on a previously described section (bimodal: fine-mode 0.21 μm, coarse-mode 2.63 μm, geometric standard deviations width 1.61 and 1.90 for fine and coarse modes, respectively, and density 1.77 g cm^{-3} [25,62]).

Fig. 5 shows the volume size distribution and extinction efficiency before and after hygroscopic growth. Dry aerosols were assigned a refractive index of 1.5 + 0.0001i.[67] After growth

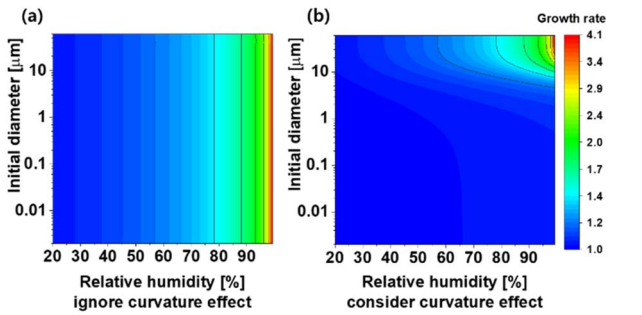

Fig. 3 Growth factor of aerosols as a function of initial aerosol size (log scale) and RH; (a) without curvature effect; (b) with curvature effect included.

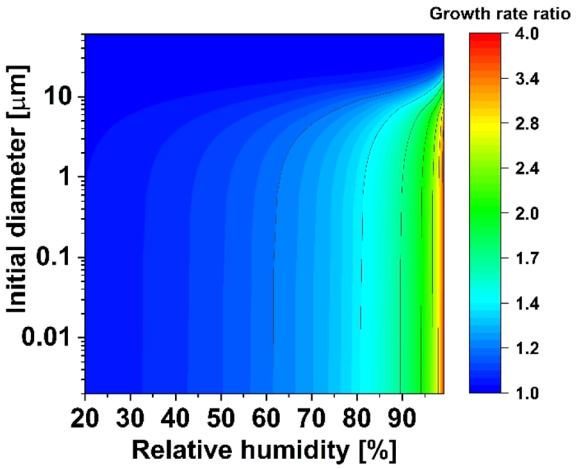

Fig. 4 Comparison of terms without and with curvature effect – the influence of the curvature effect term on the hygroscopic growth factor.

at RH = 95% ($\kappa = 0.53$), the effective refractive index was recalculated as a volume-weighted average of solute and water (eqn (4). Hygroscopic water uptake lowered the refractive index, making particles optically "smaller" than their geometric size. As a result, the extinction efficiency peak shifted to larger radii while its magnitude decreased. The volume distribution broadened and shifted to larger sizes in both fine- and coarse-modes. Extinction coefficients increased from 169.18 × 10^{-6} m^{-1} (dry) to 1161.93 × 10^{-6} m^{-1} (95% RH).

Fig. 6 presents extinction coefficients at 459, 534, and 600 nm and the corresponding AE. At low RH, extinction was mainly wavelength-dependent. Above ~98% RH, the extinction at 459 nm diverged from the other wavelengths, producing negative AE values. This indicates that at short wavelengths, extinction efficiency peaked earlier and then declined as particle growth continued.

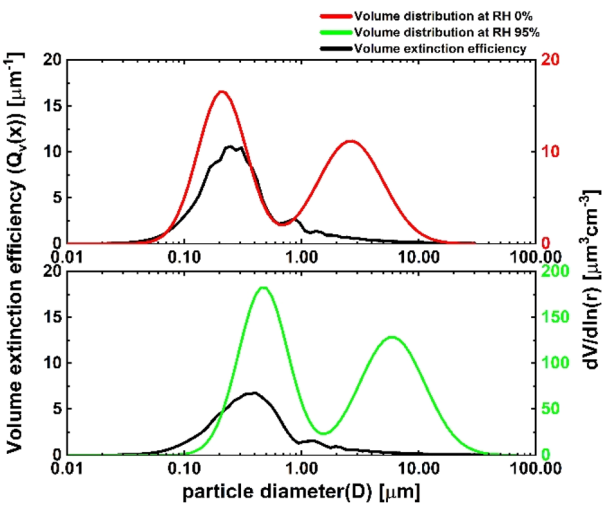

Fig. 5 Aerosol volume size distribution and volume extinction efficiency at 534 nm: (a) before hygroscopic growth; (b) at 95% RH.

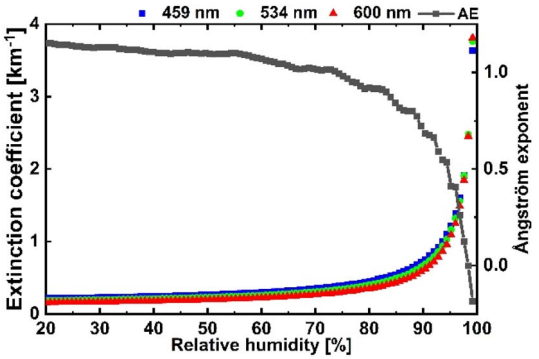

Fig. 6 Extinction coefficients and AE as a function of RH at 600, 534, and 459 nm.

For dry aerosol distribution, extinction coefficients at the three wavelengths reversed order at RH$\sim$ 0.98, causing AE <0. As shown in Fig. 2, extinction efficiency peaks at different radii for each wavelength. As particle growth shifted the size distribution, the extinction coefficient at 600 nm began to exceed that at 459 nm. This wavelength-dependent reversal resulted in negative AE values, which is characteristic of larger, hygroscopically grown particles.

Real-time monitoring of aerosol optical properties during hygroscopic growth

Fig. 7a shows extinction coefficients and AE at the R (600 nm), G (534 nm), and B (459 nm) wavelengths. While Fig. 7c presents a magnified view for RH = 93–97%. The arrows in each panel mark the temporal sequence of observations. The key findings were that near saturation (RH $\sim$ 100%), most aerosols—including coarse fog droplets—exhibited hygroscopic growth. As RH decreased over time, aerosol size decreased as well, reversing the growth process.

Grown aerosols displayed a lower extinction coefficient at shorter wavelengths compared with longer wavelengths. As aerosols shrank, the original ordering was restored, with extinction at shorter wavelengths increasing again. Similarly, AE, which reflects aerosol size, approached zero or became negative under hygroscopic growth, but returned to positive values once aerosols dried. Fig. 7b shows the temporal variations of RH and temperature. During the short period of fog droplet drying (07 : 00–09 : 00 KST), RH remained relatively constant despite a steady increase in temperature (Fig. 7d). This phenomenon occurs because water evaporates from aerosols after hygroscopic growth as temperature increases, offsetting RH changes.

Around 09 : 00 KST, evaporation slowed, and RH began to decline. As aerosols lost water, AE became positive again. Notably, RH did not decrease linearly: it first increased slightly before dropping. This reflects the balance between evaporation and warming. During this stage, the atmospheric energy budget limited the temperature rise to $\sim$1 °C per hour, slower than the subsequent $\sim$2.7 °C per hour increase later in the day.

Fig. 7c further shows that extinction coefficients decreased steadily over time. In contrast, RH followed a nonlinear increase–decrease pattern. These patterns illustrate the coupled effects of aerosol water loss and atmospheric heating. To assess whether changes in aerosol composition or size distribution contributed to the observed optical variation, $PM_{2.5}$ and PM_{10} concentrations were examined from a nearby monitoring station located 820 m from the observation site. The station is situated in a residential area with no significant emission sources, minimizing the likelihood of rapid compositional changes during the observation period. PM_{10} and $PM_{2.5}$ concentrations remained relatively stable throughout the fog episode, with mean $\pm$ standard deviation values of 61.5 $\pm$ 8.9 8 μg m^{-3}, and 38.7 $\pm$ 7.8 μg m^{-3}, respectively. These relatively small standard deviations suggest that bulk aerosol loading did not change significantly, supporting the interpretation that the observed optical variations were primarily driven by hygroscopic growth rather than changes in aerosol composition or number concentration.

Fig. 8 compares AE from image observations (blue squares) with simulations (black triangles). Observed AE values were averaged within 1% RH bins to reduce scatter, with error bars representing the range (maximum and values) of AE measurements within each RH bin. Both show the same trend: AE

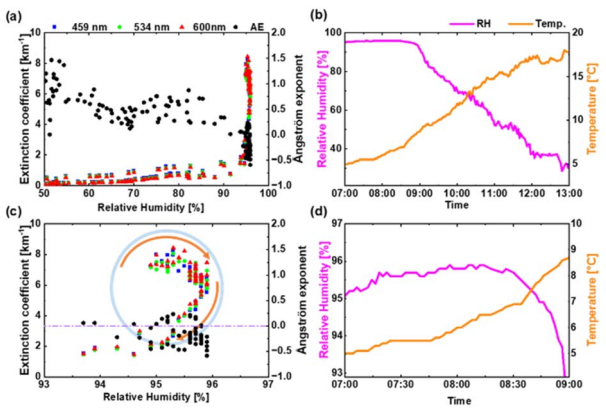

Fig. 7 Observations from November 2, 2022: (a) extinction coefficients at different wavelengths and AE as a function of RH over the full range. (b) Temporal variations in RH and temperature over the entire period. (c) Extinction coefficients and AE in the RH range at 07:00–13:00. (d) Temporal variations in RH and temperature at 07:00–13:00.

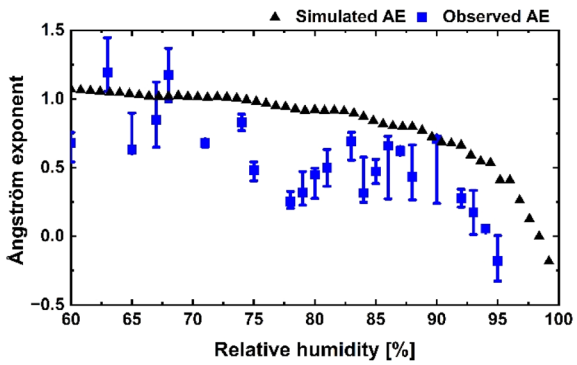

Fig. 8 Comparison of simulated and observed AE as a function of RH.

decreases under high RH, consistent with hygroscopic aerosol growth. This agreement supports the interpretation that AE variations are primarily driven by humidity effects. Because the image data (2 min interval) and KMA RH/temperature data (5 min interval) were not perfectly aligned, each image was paired with the nearest RH/temperature record (maximum offset ~2.5 min). This small mismatch may explain minor differences in AE.

In this study, the maximum measured RH was 95.9%, which likely corresponded to saturation despite not reaching 100% numerically. RH values above ~95% are generally considered saturated, and the observed fog during this period supports this interpretation.[68,69] The absence of RH values above 96% is not evidence of drying but reflects the behavior of fog: once fog forms, RH stabilizes near saturation.[70]

Conclusions

This study analyzed the hygroscopic growth characteristics of dry aerosols to better understand discrepancies between remote sensing and *in situ* measurements. Hygroscopic growth alters fundamental aerosol properties such as density, morphology, and the refractive index. Consequently, the states of dry and humidified aerosols differ depending on how humidity is controlled during measurement. To establish a common standard for quantitative evaluation, it is necessary to convert dry aerosols to a humidified state and compare them on the same basis. In this process, multiple factors were considered, including water activity, Kelvin effect, aerosol size, chemical composition (hygroscopicity), temperature, and solute molarity. An iterative approach was applied to incorporate curvature effects and analyze changes in aerosol size and surface tension.

A key characteristic of fine-mode aerosols is that the effect of the curvature cannot be neglected. For particles smaller than 1 μm, growth factors were 1.04 to 3.85 times different at RH > 90% depending on whether curvature effects were included, making curvature the dominant contributor to the hygroscopic growth of fine-mode particles. Thus, aerosol growth is determined jointly by water activity and curvature. Fine-mode growth substantially affected aerosol size and extinction efficiency, strongly influencing the overall extinction coefficient. In contrast, coarse-mode aerosols had minimal impact because their relative volume extinction efficiency decreases despite volume growth. These results confirm that fine- and coarse-mode aerosols exhibit different hygroscopic behaviors, with fine-mode aerosols exerting the strongest influence on light extinction.

In remote sensing, the extinction coefficient depends on the aerosol size and refractive index. As aerosols grow, water increases their volume but simultaneously lowers their refractive index toward that of water ($n = 1.33$). This counteracts exponential increases in extinction that might otherwise result from volume growth. According to Mie theory, extinction efficiency varies with both size and wavelength. As aerosols grow, AE generally decreases—a trend confirmed by observations. In our camera observations, AE even became negative at RH ~92%. Discrepancies between simulations and measurements were attributed to uncertainties in the dry aerosol size distribution and κ. Smaller dry sizes or lower hygroscopicity shift the extinction reversal to higher RH, showing that the RH threshold for negative AE is governed primarily by fine-mode modal size and κ. Thus, the dry size distribution can be used to predict the RH at which wavelength-dependent extinction reversal occurs.

Field observations confirmed the effects of hygroscopic growth on aerosol extinction. At high RH, aerosols—including fog droplets—grew substantially, reducing AE and shifting extinction behavior. As RH decreased, water evaporated and aerosols shrank. Consequently, extinction at shorter wavelengths increased, and AE returned to positive values. The results also demonstrated nonlinear RH-temperature dynamics: as temperature rose, RH initially remained steady because evaporation absorbed thermal energy, slowing temperature rise. Once evaporation ceased, RH declined and extinction properties shifted accordingly. The observed evolution of extinction coefficients and AE retrieved from RGB camera images (Fig. 7.) was broadly consistent with the Mie-theory simulations presented in Fig. 6. In both cases, extinction at shorter wavelengths decreased relative to longer wavelengths as RH increased, and AE approached zero or become negative under high-humidity conditions before recovering as aerosols dried. These agreements suggest that the wavelength-dependent optical changes observed during the fog episode can be primarily attributed to hygroscopic particle growth, rather than changes in aerosol composition or emission sources. This demonstrates that image-based methods can effectively capture real-time aerosol hygroscopic behavior. The approach provides a cost-effective tool for validating growth models and monitoring aerosol–humidity interactions under ambient atmospheric conditions.

Future research should test this method under diverse atmospheric conditions and regions to derive representative κ. If instruments such as Optical Particle Counter or a Scanning Mobility Particle Sizer are used to measure dry aerosol size distributions, unknown regional κ and refractive indices could be estimated inversely. Because RH and κ are known, our approach can run in "inverse mode": retrieving the dry size distribution from image-derived extinction. Fitting a bimodal distribution to match observed extinction at measured RH would allow particle size distribution retrievals from images alone. This capability would enable locally tailored predictions of visibility and AE. Continued efforts should focus on characterizing regional variations and improving predictive model accuracy based on these findings.

Author contributions

J. Sim and D. K. developed the simulation; D. K., J. Shin and S. J. conducted the measurements; J. Sim, J. Shin, D. K. and Y. N. analyzed the data; J. Sim, J. Shin and Y. M. prepared the manuscript draft; J. Sim, J. Shin, Y. M., N. D., S. J., D. K., and Y. N. reviewed and revised the manuscript.

Conflicts of interest

There are no conflicts to declare.

Data availability

The data supporting the findings of this study are stored in a private GitHub repository (https://github.com/juhyeon1012/ESPI_HygroscopicGrowth) and are available from the corresponding author upon reasonable request.

Acknowledgements

This research was supported by the Basic Science Research Program through the National Research Foundation of Korea (NRF) funded by the Ministry of Education (No. RS-2025-25411926).

References

1 J.-P. Chen, Theory of deliquescence and modified Köhler curves, *J. Atmos. Sci.*, 1994, **51**, 3505–3516.
2 V. A. Lanz, A. S. H. Prévôt, M. R. Alfarra, S. Weimer, C. Mohr, P. F. DeCarlo, M. F. D. Gianini, C. Hueglin, J. Schneider, O. Favez, B. D'Anna, C. George and U. Baltensperger, Characterization of aerosol chemical composition with aerosol mass spectrometry in Central Europe: an overview, *Atmos. Chem. Phys.*, 2010, **10**, 10453–10471.
3 L. Schmeisser, E. Andrews, J. A. Ogren, P. Sheridan, A. Jefferson, S. Sharma, J. E. Kim, J. P. Sherman, M. Sorribas, I. Kalapov, T. Arsov, C. Angelov, O. L. Mayol-Bracero, C. Labuschagne, S.-W. Kim, A. Hoffer, N.-H. Lin, H.-P. Chia, M. Bergin, J. Sun, P. Liu and H. Wu, Classifying aerosol type using in situ surface spectral aerosol optical properties, *Atmos. Chem. Phys.*, 2017, **17**, 12097–12120.
4 A. Mhawish, M. Sorek-Hamer, R. Chatfield, T. Banerjee, M. Bilal, M. Kumar, C. Sarangi, M. Franklin, K. Chau, M. Garay and O. Kalashnikova, Aerosol characteristics from earth observation systems: A comprehensive investigation over South Asia (2000–2019), *Rem. Sens. Environ.*, 2021, 259.
5 T. Wu and B. E. Boor, Urban aerosol size distributions: a global perspective, *Atmos. Chem. Phys.*, 2021, **21**, 8883–8914.
6 H. Yoo, L. Wu, H. Geng and C. U. Ro, Physicochemical and temporal characteristics of individual atmospheric aerosol particles in urban Seoul during KORUS-AQ campaign: insights from single-particle analysis, *Atmos. Chem. Phys.*, 2024, **24**, 853–867.
7 H. Köhler, The nucleus in and the growth of hygroscopic droplets, *Trans. Faraday Soc.*, 1936, **32**, 1152–1161.
8 M. Petters and S. Kreidenweis, A single parameter representation of hygroscopic growth and cloud condensation nucleus activity, *Atmos. Chem. Phys.*, 2007, **7**, 1961–1971.
9 E. Swietlicki, H.-C. Hansson, K. Hämeri, B. Svenningsson, A. Massling, G. McFiggans, P. H. McMurry, T. Petäjä, P. Tunved and M. Gysel, Hygroscopic properties of submicrometer atmospheric aerosol particles measured with H-TDMA instruments in various environments—a review, *Tellus B*, 2008, **60**, 432–469.
10 I. N. Tang and H. R. Munkelwitz, Composition and temperature dependence of the deliquescence properties of hygroscopic aerosols, *Atmos. Environ. Part A Gen. Top.*, 1993, **27**, 467–473.
11 I. Tang and H. Munkelwitz, Water activities, densities, and refractive indices of aqueous sulfates and sodium nitrate droplets of atmospheric importance, *J. Geophys. Res. Atmos.*, 1994, **99**, 18801–18808.
12 S. Kreidenweis, K. Koehler, P. DeMott, A. Prenni, C. Carrico and B. Ervens, Water activity and activation diameters from hygroscopicity data-Part I: Theory and application to inorganic salts, *Atmos. Chem. Phys.*, 2005, **5**, 1357–1370.
13 S. Gunthe, S. King, D. Rose, Q. Chen, P. Roldin, D. Farmer, J. Jimenez, P. Artaxo, M. O. Andreae and S. Martin, Cloud condensation nuclei in pristine tropical rainforest air of Amazonia: size-resolved measurements and modeling of atmospheric aerosol composition and CCN activity, *Atmos. Chem. Phys.*, 2009, **9**, 7551–7575.
14 D. Rose, A. Nowak, P. Achtert, A. Wiedensohler, M. Hu, M. Shao, Y. Zhang, M. Andreae and U. Pöschl, Cloud condensation nuclei in polluted air and biomass burning smoke near the mega-city Guangzhou, China–Part 1: Size-resolved measurements and implications for the modeling of aerosol particle hygroscopicity and CCN activity, *Atmos. Chem. Phys.*, 2010, **10**, 3365–3383.
15 M. Paramonov, P. Aalto, A. Asmi, N. Prisle, V.-M. Kerminen, M. Kulmala and T. Petäjä, The analysis of size-segregated cloud condensation nuclei counter (CCNC) data and its implications for cloud droplet activation, *Atmos. Chem. Phys.*, 2013, **13**, 10285–10301.
16 G. Mie, Beiträge zur Optik trüber Medien, speziell kolloidaler Metallösungen, *Ann. Phys.*, 1908, **330**, 377–445.
17 M. I. Mishchenko, L. D. Travis and A. A. Lacis, in. *Scattering, Absorption, and Emission of Light by Small Particles*, Cambridge university press, 2002.
18 C. F. Bohren and D. R. Huffman, in. *Absorption and Scattering of Light by Small Particles*, John Wiley & Sons, 2008.
19 A. Ångström, On the atmospheric transmission of sun radiation and on dust in the air, *Geogr. Ann.*, 1929, **11**, 156–166.
20 T. F. Eck, B. Holben, J. Reid, O. Dubovik, A. Smirnov, N. O'neill, I. Slutsker and S. Kinne, Wavelength dependence of the optical depth of biomass burning, urban, and desert dust aerosols, *J. Geophys. Res. Atmos.*, 1999, **104**, 31333–31349.
21 G. L. Schuster, O. Dubovik and B. N. Holben, Angstrom exponent and bimodal aerosol size distributions, *J. Geophys. Res. Atmos.*, 2006, **111**, D07207.
22 G. Gobbi, Y. Kaufman, I. Koren and T. Eck, Classification of aerosol properties derived from AERONET direct sun data, *Atmos. Chem. Phys.*, 2007, **7**, 453–458.
23 D. Kaskaoutis, H. Kambezidis, N. Hatzianastassiou, P. Kosmopoulos and K. Badarinath, Aerosol climatology: dependence of the Angstrom exponent on wavelength over four AERONET sites, *Atmos. Chem. Phys. Discuss.*, 2007, **7**, 7347–7397.

24 G. Hänel, in *Advances in Geophysics*, Elsevier, 1976, vol. 19, pp. 73–188.
25 I. N. Tang, Chemical and size effects of hygroscopic aerosols on light scattering coefficients, *J. Geophys. Res. Atmos.*, 1996, **101**, 19245–19250.
26 R. Fierz-Schmidhauser, P. Zieger, M. Gysel, L. Kammermann, P. F. DeCarlo, U. Baltensperger and E. Weingartner, Measured and predicted aerosol light scattering enhancement factors at the high alpine site Jungfraujoch, *Atmos. Chem. Phys.*, 2010, **10**, 2319–2333.
27 P. Zieger, E. Weingartner, J. Henzing, M. Moerman, G. De Leeuw, J. Mikkilä, M. Ehn, T. Petäjä, K. Clémer and M. Van Roozendael, Comparison of ambient aerosol extinction coefficients obtained from in-situ, MAX-DOAS and LIDAR measurements at Cabauw, *Atmos. Chem. Phys.*, 2011, **11**, 2603–2624.
28 M. Gysel, J. Crosier, D. Topping, J. Whitehead, K. Bower, M. Cubison, P. Williams, M. Flynn, G. McFiggans and H. Coe, Closure study between chemical composition and hygroscopic growth of aerosol particles during TORCH2, *Atmos. Chem. Phys.*, 2007, **7**, 6131–6144.
29 N. Good, D. Topping, J. Allan, M. Flynn, E. Fuentes, M. Irwin, P. Williams, H. Coe and G. McFiggans, Consistency between parameterisations of aerosol hygroscopicity and CCN activity during the RHaMBLe discovery cruise, *Atmos. Chem. Phys.*, 2010, **10**, 3189–3203.
30 D. S. Covert, R. Charlson and N. Ahlquist, A study of the relationship of chemical composition and humidity to light scattering by aerosols, *J. Appl. Meteorol. Climatol.*, 1972, **11**, 968–976.
31 C. M. Carrico, P. Kus, M. J. Rood, P. K. Quinn and T. S. Bates, Mixtures of pollution, dust, sea salt, and volcanic aerosol during ACE-Asia: Radiative properties as a function of relative humidity, *J. Geophys. Res. Atmos.*, 2003, **108**(D23), 8650.
32 J. H. Seinfeld and S. N. Pandis, in. *Atmospheric Chemistry and Physics: from Air Pollution to Climate Change*, John Wiley & Sons, 2016.
33 H. Wex, M. D. Petters, C. M. Carrico, E. Hallbauer, A. Massling, G. R. McMeeking, L. Poulain, Z. Wu, S. M. Kreidenweis and F. Stratmann, Towards closing the gap between hygroscopic growth and activation for secondary organic aerosol: Part 1 – Evidence from measurements, *Atmos. Chem. Phys.*, 2009, **9**, 3987–3997.
34 D. O. Topping, G. McFiggans and H. Coe, A curved multi-component aerosol hygroscopicity model framework: Part 1–Inorganic compounds, *Atmos. Chem. Phys.*, 2005, **5**, 1205–1222.
35 E. Mikhailov, S. Vlasenko, S. Martin, T. Koop and U. Pöschl, Amorphous and crystalline aerosol particles interacting with water vapor: conceptual framework and experimental evidence for restructuring, phase transitions and kinetic limitations, *Atmos. Chem. Phys.*, 2009, **9**, 9491–9522.
36 N. L. Prisle, T. Raatikainen, A. Laaksonen and M. Bilde, Surfactants in cloud droplet activation: mixed organic-inorganic particles, *Atmos. Chem. Phys.*, 2010, **10**, 5663–5683.
37 C. R. Ruehl, J. F. Davies and K. R. Wilson, An interfacial mechanism for cloud droplet formation on organic aerosols, *Science*, 2016, **351**, 1447–1450.
38 R. Sorjamaa, B. Svenningsson, T. Raatikainen, S. Henning, M. Bilde and A. Laaksonen, The role of surfactants in Köhler theory reconsidered, *Atmos. Chem. Phys.*, 2004, **4**, 2107–2117.
39 A. Nenes and J. H. Seinfeld, Parameterization of cloud droplet formation in global climate models, *J. Geophys. Res. Atmos.*, 2003, **108**(D14), 4415.
40 M. Mazoyer, F. Burnet, C. Denjean, G. C. Roberts, M. Haeffelin, J. C. Dupont and T. Elias, Experimental study of the aerosol impact on fog microphysics, *Atmos. Chem. Phys.*, 2019, **19**, 4323–4344.
41 A. Bott, Comparison of a spectral microphysics and a two-moment cloud scheme: Numerical simulation of a radiation fog event, *Atmos. Res.*, 2021, 262.
42 W. Xu, Y. Kuang, W. Xu, Z. Zhang, B. Luo, X. Zhang, J. Tao, H. Qiao, L. Liu and Y. Sun, Hygroscopic growth and activation changed submicron aerosol composition and properties in the North China Plain, *Atmos. Chem. Phys.*, 2024, **24**, 9387–9399.
43 A. Ångström, The parameters of atmospheric turbidity, *Tellus*, 1964, **16**, 64–75.
44 K. He, J. Sun and X. Tang, Single Image Haze Removal Using Dark Channel Prior, *IEEE Trans. Pattern Anal. Mach. Intell.*, 2011, **33**, 2341–2353.
45 S. Park and D. Kim, Aerosol-extinction retrieval method at three effective RGB wavelengths using a commercial digital camera, *Korean J. Opt. Photon.*, 2020, **31**, 71–80.
46 D. Kim and Y. Noh, An aerosol extinction coefficient retrieval method and characteristics analysis of landscape images, *Sensors*, 2021, **21**, 7282.
47 J. Shin, D. Kim and Y. Noh, Estimation of Aerosol Extinction Coefficient Using Camera Images and Application in Mass Extinction Efficiency Retrieval, *Remote Sens.*, 2022, **14**, 1224.
48 R. Szeliski, in. *Computer Vision: Algorithms and Applications*, Springer Nature, 2022.
49 H. R. Pruppacher, J. D. Klett and P. K. Wang, Microphysics of clouds and precipitation. 1998.
50 E. Mikhailov, S. Vlasenko, R. Niessner and U. Pöschl, Interaction of aerosol particles composed of protein and salts with water vapor: hygroscopic growth and microstructural rearrangement, *Atmos. Chem. Phys.*, 2004, **4**, 323–350.
51 D. Rose, S. Gunthe, E. Mikhailov, G. Frank, U. Dusek, M. O. Andreae and U. Pöschl, Calibration and measurement uncertainties of a continuous-flow cloud condensation nuclei counter (DMT-CCNC): CCN activation of ammonium sulfate and sodium chloride aerosol particles in theory and experiment, *Atmos. Chem. Phys.*, 2008, **8**, 1153–1179.
52 M. Petters and S. Kreidenweis, A single parameter representation of hygroscopic growth and cloud condensation nucleus activity–Part 2: Including solubility, *Atmos. Chem. Phys.*, 2008, **8**, 6273–6279.

53 A. Abo Riziq, C. Erlick, E. Dinar and Y. Rudich, Optical properties of absorbing and non-absorbing aerosols retrieved by cavity ring down (CRD) spectroscopy, *Atmos. Chem. Phys.*, 2007, **7**, 1523–1536.
54 R. E. Miles, S. Rudic, A. J. Orr-Ewing and J. P. Reid, Influence of uncertainties in the diameter and refractive index of calibration polystyrene beads on the retrieval of aerosol optical properties using cavity ring down spectroscopy, *J. Phys. Chem.*, 2010, **114**, 7077–7084.
55 S. M. Kreidenweis, M. D. Petters and P. J. DeMott, Single-parameter estimates of aerosol water content, *Environ. Res. Lett.*, 2008, **3**, 035002.
56 I. Svenningsson, H. C. Hansson, A. Wiedensohler, J. Ogren, K. Noone and A. Hallberg, Hygroscopic growth of aerosol particles in the Po Valley, *Tellus B*, 1992, **44**, 556–569.
57 T. V. Vu, J. M. Delgado-Saborit and R. M. Harrison, A review of hygroscopic growth factors of submicron aerosols from different sources and its implication for calculation of lung deposition efficiency of ambient aerosols, *Air Qual. Atmos. Health*, 2015, **8**, 429–440.
58 W. C. Malm, B. A. Schichtel, M. L. Pitchford, L. L. Ashbaugh and R. A. Eldred, Spatial and monthly trends in speciated fine particle concentration in the United States, *J. Geophys. Res. Atmos.*, 2004, **109**, D03306.
59 J.-P. Putaud, R. Van Dingenen, A. Alastuey, H. Bauer, W. Birmili, J. Cyrys, H. Flentje, S. Fuzzi, R. Gehrig and H.-C. Hansson, A European aerosol phenomenology–3: Physical and chemical characteristics of particulate matter from 60 rural, urban, and kerbside sites across Europe, *Atmos. Environ.*, 2010, **44**, 1308–1320.
60 S.-M. Park, I.-H. Song, J. S. Park, J. Oh, K. J. Moon, H. J. Shin, J. Y. Ahn, M.-D. Lee, J. Kim and G. Lee, Variation of $PM_{2.5}$ chemical compositions and their contributions to light extinction in Seoul, *Aerosol Air Qual. Res.*, 2018, **18**, 2220–2229.
61 I. Bulatovic, A. L. Igel, C. Leck, J. Heintzenberg, I. Riipinen and A. M. L. Ekman, The importance of Aitken mode aerosol particles for cloud sustenance in the summertime high Arctic – a simulation study supported by observational data, *Atmos. Chem. Phys.*, 2021, **21**, 3871–3897.
62 G. Choudhury and M. Tesche, A first global height-resolved cloud condensation nuclei data set derived from spaceborne lidar measurements, *Earth Syst. Sci. Data*, 2023, **15**, 3747–3760.
63 J.-P. Putaud, R. Van Dingenen, M. Mangoni, A. Virkkula, F. Raes, H. Maring, J. Prospero, E. Swietlicki, O. Berg and R. Hillamo, Chemical mass closure and assessment of the origin of the submicron aerosol in the marine boundary layer and the free troposphere at Tenerife during ACE-2, *Tellus B*, 2000, **52**, 141–168.
64 J. L. Hand and S. M. Kreidenweis, A New Method for Retrieving Particle Refractive Index and Effective Density from Aerosol Size Distribution Data, *Aerosol Sci. Technol.*, 2002, **36**, 1012–1026.
65 R. P. Damadeo, V. F. Sofieva, A. Rozanov and L. W. Thomason, An empirical characterization of the aerosol Ångström exponent interpolation bias using SAGE III/ISS data, *Atmos. Meas. Tech.*, 2024, **17**, 3669–3678.
66 R. Jaenicke, Natural aerosols, *Ann. N. Y. Acad. Sci.*, 1980, **338**, 317–329.
67 O. B. Toon, J. B. Pollack and B. N. Khare, The optical constants of several atmospheric aerosol species: Ammonium sulfate, aluminum oxide, and sodium chloride, *J. Geophys. Res.*, 1976, **81**, 5733–5748.
68 O. Klemm and N.-H. Lin, What causes observed fog trends: Air quality or climate change?, *Aerosol Air Qual. Res.*, 2016, **16**, 1131–1142.
69 L. Jia, Y. Xu and M. Duan, Explosive formation of secondary organic aerosol due to aerosol-fog interactions, *Sci. Total Environ.*, 2023, **866**, 161338.
70 A. Gandhi, I. Geresdi, A. Z. Gyöngyösi, Á. V. Tordai, P. Torma, A. Rehak, M. Bíró-Szilágyi, G. Horvath, Z. Ferenczi and K. Imre, An Observational Case Study of a Radiation Fog Event, *Pure Appl. Geophys.*, 2024, **181**, 2025–2049.

